

# Structural, magnetic, and electronic diversity of VTe<sub>2</sub> monolayer

Bi-Dan Guo, Ji-Hai Liao, Wen-Qiang Xie, Yin-Hui Peng, Yu-Jun Zhao\*



Department of Physics, South China University of Technology, Guangzhou 510640, People's Republic of China

## ARTICLE INFO

### Article history:

Received 15 March 2022

Received in revised form 29 May 2022

Accepted 8 June 2022

Available online 16 June 2022

Communicated by L. Woods

### Keywords:

Two-dimensional

Ferrimagnetic half-metal

Antiferromagnetic metal

Antiferromagnetic semiconductor

Phase transition

## ABSTRACT

Two-dimensional transition metal dichalcogenides (TMDs) exhibit many novel properties due to dimension, lattice distortion, electron-electron interaction etc. Here, we determine that 1T-VTe<sub>2</sub> with space group  $P\bar{3}m1$  is an antiferromagnetic metal by first-principles calculations, and three metastable structures are predicted, i.e., the  $P21/m$  and  $C2/m$  antiferromagnetic semiconductor phases and  $P3m1$  ferrimagnetic half-metal phase. Besides, the  $C2/m$  phase can be transferred to the  $P3m1$  phase by electron doping, while hole doping can induce a transition from  $C2/m$  phase to  $P\bar{3}m1$  phase. These transitions could be ascribed to a strong coupling of charge, lattice, and spin degrees of freedom in VTe<sub>2</sub>. The diverse electronic and magnetic properties of VTe<sub>2</sub> provide a good platform for researchers to understand the interactions between spin, charge and lattice.

© 2022 Elsevier B.V. All rights reserved.

## 1. Introduction

Two-dimensional (2D) magnetic materials with many peculiar properties have caused extensive concern of the scientific research workers for both fundamental physics and potential applications in spintronics [1]. Since intrinsic magnetism was first experimentally observed in CrI<sub>3</sub> monolayers [2]. Tremendous efforts have been made to explore other 2D materials with intrinsic magnetism and explore novel features in them. For example, transition metal dichalcogenides (TMDs) have attracted broad interest due to their unique properties, such as superconductivity [3,4], valley polarization [5,6], Dirac semimetal [7,8], charge density wave [9,10], Kondo effect [11,12], giant magnetoresistance effect [13,14] and so on, which are useful for potential applications in integrated circuits, valleytronics, magnetic sensors and memory devices [15–18].

As an important member of TMDs, VTe<sub>2</sub> mainly exhibits two polymorphs, i.e., the 2H phase (trigonal prismatic coordination) or 1T phase (octahedral coordination) [19,20]. First-principles study predicted that the 1T-VTe<sub>2</sub> is more energetically favorable than 2H phase and has a ferromagnetic ground state [13,20,21]. Ultrathin 1T-VTe<sub>2</sub> nanoplates were successfully synthesized and were reported to behave room temperature ferromagnetism [22]. However, no ferromagnetic order was observed in a high-quality monolayer VTe<sub>2</sub> film, recently grown on bilayer graphene by the molecular-beam-epitaxy (MBE) method [23]. Especially, Liu *et al.* demonstrated that 1-VTe<sub>2</sub> monolayers appear (4 × 4) metallic and gaped

( $2\sqrt{3} \times 2\sqrt{3}$ ) charge density wave (CDW) phase [9]. The CDW-driven reorganization of the atomic structure weakens the ferromagnetic super-exchange coupling and strengthens the antiferromagnetic exchange coupling, suppressing the long-range magnetic order [24]. More interestingly, the spin, charge, and lattice degrees of freedom are strongly coupled in the single crystal VTe<sub>2</sub>, which induces two types of CDW phases with different antiferromagnetic spin orderings [25]. In short, due to the complex interactions between spin, charge, and lattices, there is no consensus on whether 1T-VTe<sub>2</sub> exist intrinsic magnetism. It is particularly important to explore the magnetic properties of 1T-VTe<sub>2</sub>.

In this work, we have investigated the electronic structures and magnetic ground states of all possible configurations of  $2 \times 2$ ,  $3 \times 3$ , and selected configurations of  $4 \times 4$  supercell of 1T-VTe<sub>2</sub> monolayer by employing first-principles calculations. The results reveal that non-distorted 1T-VTe<sub>2</sub> exhibits antiferromagnetic metallicity, in sharp contrast to the earlier reported ferromagnetic ground state [13,21], which was concluded from only two magnetic configurations in a  $2 \times 2$  cell. When the symmetry limitation is released, three different VTe<sub>2</sub> phases,  $P3m1$ ,  $P21/m$ , and  $C2/m$  appear, coupling with various magnetic state and electronic structures. Furthermore, VTe<sub>2</sub> can be transformed from  $C2/m$  antiferromagnetic semiconductor to  $P\bar{3}m1$  ferrimagnetic metal by electron doping while hole doping can induce a transition from  $C2/m$  antiferromagnetic semiconductor to  $P\bar{3}m1$  antiferromagnetic metal. Such diversified magnetism and electronic properties in VTe<sub>2</sub> monolayers reflect the strong coupling between the charge, spin, and lattice.

\* Corresponding author.

E-mail address: zhaoyj@scut.edu.cn (Y.-J. Zhao).

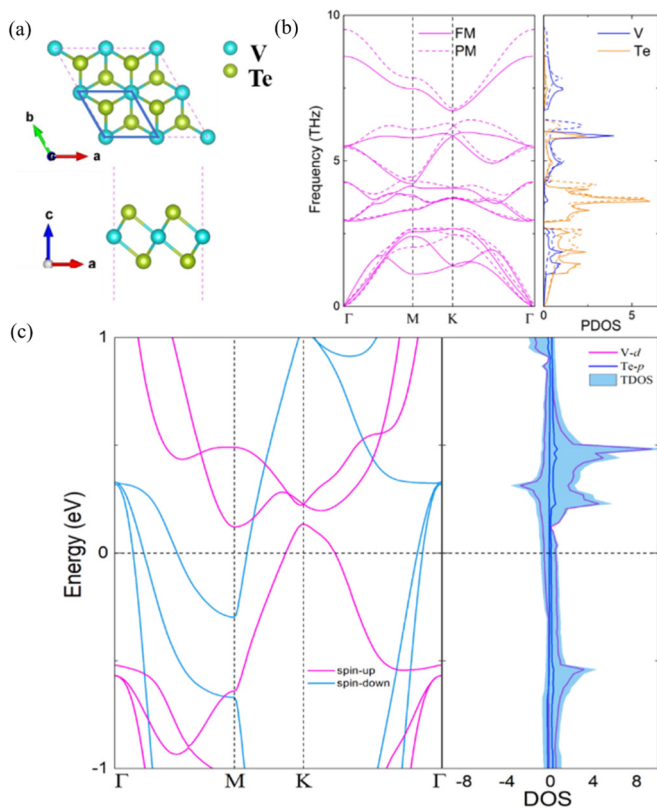


**Fig. 1.** (a) Crystal structures of 1T-VTe<sub>2</sub> monolayer, the solid blue lines represent a primitive cell. (b) Phonon spectra (left) and partial density of states (right) of FM state (solid line) and PM state (dotted line). (c) Electronic band structures (left) and the total and partial electron density of states (right) of 1T-VTe<sub>2</sub> primitive cell. (For interpretation of the colors in the figure(s), the reader is referred to the web version of this article.)

## 2. Computational details

The calculations are conducted with the Vienna *ab initio* Simulation Package (VASP) [26,27] with a plane-wave basis set by using the projector augmented wave (PAW) method [28,29]. The exchange correlation interactions are described by the generalized gradient approximation (GGA) in the formalism of Perdew-Burke-Ernzerhof (PBE) [30]. A plane wave energy cutoff energy of 500 eV is used. The Gamma-centered k-point meshes are chosen as  $25 \times 25 \times 1$ ,  $8 \times 8 \times 1$ ,  $6 \times 6 \times 1$  and  $4 \times 4 \times 1$  for 1T-VTe<sub>2</sub> primitive-cell,  $2 \times 2 \times 1$ ,  $3 \times 3 \times 1$  and  $4 \times 4 \times 1$  supercells, respectively. The convergence criteria for energy and force are set to be  $1 \times 10^{-6}$  eV and 0.01 eV/Å, respectively. To avoid the interaction between adjacent layers, a vacuum space of 16 Å is used along the z-axis. We employed a noncollinear total energy calculation with spin-orbit coupling (SOC) to determine the magnetization direction. To check the structural stability, the phonon frequencies were calculated by using density functional perturbation theory (DFPT) method [31] and assisted by PHONOPY [32] code. VASPKIT [33] program was used for electronic structure data processing. The enumeration of Wyckoff sites was performed by home made structural search software SAGAR [34].

## 3. Results and discussion

### 3.1. Structure and magnetic ordering

The structure of monolayer 1T-VTe<sub>2</sub> is presented in Fig. 1a, which consists of three atomic layers with the vanadium layer sandwiched by two tellurium layers. It has octahedral coordination

and belong to the space group of  $P\bar{3}m1$  (No. 164). For the primitive cell, the structure was optimized with spin (ferromagnetic (FM)) or without spin (paramagnetic (PM)) polarization, respectively. The FM state possesses a much lower energy than the PM state, and its lattice constant (3.59 Å) and total magnetic moment (0.79  $\mu_B$ ) are consistent with previous research results [13,22]. The effect of spin-lattice coupling is firstly reflected in the structural changes and then in the lattice vibrations. As listed in Table S1 in the Supplementary Material, the lattice constant changes from 3.55 to 3.59 Å (increase by 1.1%), and the bond lengths and the bond angles change significantly. The phonon dispersions and partial density of states for FM state and PM state are shown in Fig. 1b, where the overall group velocity for optical phonon branches of FM ordering is much less than that of PM ordering. Besides, the phonon bandgap of FM is enlarged as the optical branches of low frequency shift down, which is also clearly shown by the partial density of states. The branches with large frequency shifts indicate that there exists strong spin-lattice coupling in VTe<sub>2</sub>.

To assess the structural stability of 1T-VTe<sub>2</sub> monolayers, we calculate their formation enthalpy by the definition of  $\Delta H = (E_{\text{system}} - mE_V - nE_{\text{Te}})/(m + n)$ , where  $E_{\text{system}}$  is the total energy of 1T-VTe<sub>2</sub> monolayer,  $E_V$  and  $E_{\text{Te}}$  is the energy of the elemental crystal of V ( $Im\bar{3}m$  phase) and Te ( $P3_121$  phase), respectively.  $m$ ,  $n$  denote the number of V and Te atoms. The calculated formation enthalpy is  $-0.296$  eV per atom, the negative formation enthalpy implies that 1T-VTe<sub>2</sub> is thermodynamically stable. Kinetic stability of the 1T-VTe<sub>2</sub> monolayer is confirmed by its phonon band dispersion (Fig. 1b), which shows no imaginary frequencies in the entire Brillouin zone. Fig. 1c shows the energy band structures and the partial density of states (PDOS) of 1T-VTe<sub>2</sub> primitive cell. Obviously, we find that the monolayer 1T-VTe<sub>2</sub> exhibits metallic natures in both spin channels. These results are consistent with earlier studies reported by Begunovich [13] et al. (a comparison is shown in Figure S4).

In order to determine the magnetic ground state of 1T-VTe<sub>2</sub>, we construct all the possible magnetic structures in  $2 \times 2$  and  $3 \times 3$  supercell, as depicted in Figure S1 and Figure S2 (see Supplementary Information). However, in a  $4 \times 4$  supercell, there are 312 magnetic configurations in total. The computational efforts for all the possible configurations in  $4 \times 4$  supercell are huge. Here we selected 12 highly symmetrical magnetic configurations according to the constraint that the Wyckoff sites do not exceed 10 (shown in Figure S3). In order to test the effects of spin lattice, we calculated relative energies  $\Delta E = E - E_{\text{FM}}$  (where  $E$  is the total energy of magnetic structure,  $E_{\text{FM}}$  is the energy of ferromagnetic (FM) state) for all the magnetic configurations using two different procedures. Procedure 1 is the static calculations using the structure optimized with FM order, and Procedure 2 is the full calculations in which the structures are optimized with the corresponding magnetic orders. The results from both procedures are shown in Fig. 2. When 1T-VTe<sub>2</sub> maintains its high symmetry (using Procedure 1), the stepped antiferromagnetic (Figure S3g or Fig. 2c, denoted by sAFM) is energetically preferable with  $\Delta E$  of  $-21.8$  meV/f.u. (shown in Fig. 2a). The earlier theoretical studies reported that 1T-VTe<sub>2</sub> is favored in FM ground state, merely considering two magnetic configurations in a  $2 \times 2$  supercell [13,21]. Furthermore, if we release the symmetry constriction of VTe<sub>2</sub>, i.e., from our fully relaxed Procedure 2 (cf. Fig. 2b), another AFM configuration (Figure S3k or Fig. 2e, denoted by zAFM) energetically prevails over the FM phase by  $-46$  meV/f.u. The magnetic configuration of VTe<sub>2</sub> is clearly sensitive to the structural relaxation, suggesting that spin-lattice coupling is strong in VTe<sub>2</sub>. More importantly, due to spin-lattice interactions, there emerges three diverse metastable phases with different magnetic states, including  $P3m1$  (156) with an Ferrimagnetic state (FerriM),  $P21/m$  (11) and  $C2/m$  (12) with dAFM and zAFM state respectively. Next we are going to focus on these three structures.

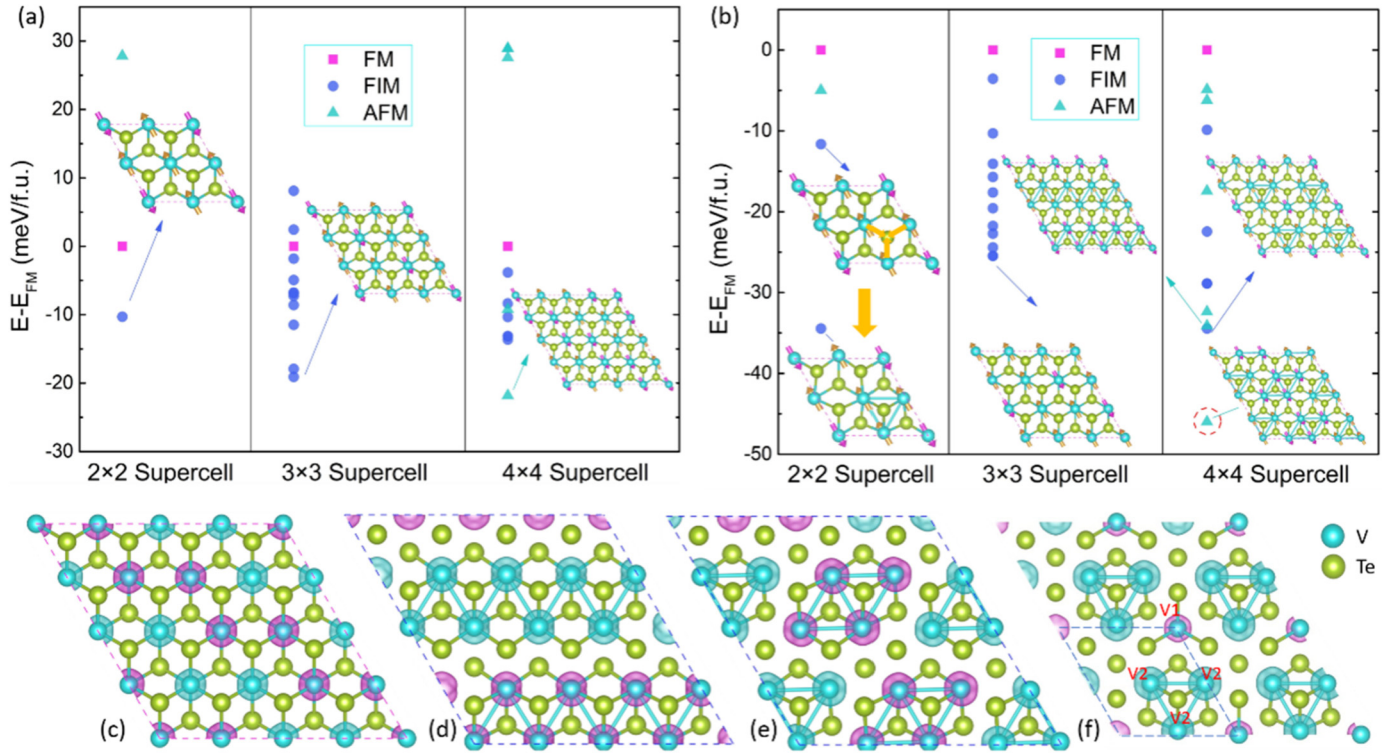


**Fig. 2.** The energy difference between different magnetic configurations in different supercells and FM for using Procedure 1 (a) and Procedure 2 (b), respectively. Red rectangle represents FM, blue circle denotes FerriM, and cyan is the AFM. The red circles indicate the ground state. (c) sAFM  $P\bar{3}m1$  phase. (d) dAFM  $P21/m$  phase. (e) zAFM  $C2/m$  phase. (f) FerriM  $P3m1$  phase. Cyan and red isosurfaces represent spin up and spin down densities, respectively. The blue dot lines represent unit cell corresponding to their magnetic state.

**Table 1**

Optimized structural parameters and the formation enthalpy of different  $VTe_2$  phases with the ground magnetic state.

Space group	Magnetic state	Lattice parameters (Å, deg)	Bond length (Å)		Angle (deg)	$\Delta H$ (eV)
			V-Te	V-V		
$P\bar{3}m1$	sAFM	$a = b = 14.35$ $\alpha = \beta = 90$ $\gamma = 120$	2.70	3.59	V-Te-V 83.25	-0.301
$P3m1$	FerriM	$a = b = 7.20$ $\alpha = \beta = 90$ $\gamma = 120$	2.73 (2.67 ~ 2.76)	3.41 (3.21 ~ 3.61)	V-Te-V 73.35 ~ 92.21	-0.305
$P21/m$	dAFM	$a = 14.24$ $b = 14.42$ $\alpha = \beta = 90$ $\gamma = 119.58$	2.72 (2.67 ~ 2.77)	3.61 (3.36 ~ 3.86)	V-Te-V 77.69 ~ 89.42	-0.305
$C2/m$	zAFM	$a = 14.35$ $b = 14.46$ $\alpha = \beta = 90$ $\gamma = 120.25$	2.71 (2.66 ~ 2.76)	3.61 (3.25 ~ 3.98)	V-Te-V 74.39 ~ 87.82	-0.309

### 3.2. Three predicted structures and their stability

The structures of three metastable phases and pure  $1T-VTe_2$  are shown in Fig. 2c-f. The structural information and formation enthalpy of different structures are summarized in Table 1. Numerically, the optimized  $C2/m$  phase with zAFM state is the most energetically stable structure. Its formation enthalpy is 13 meV/f.u. lower than that of the  $P\bar{3}m1$  phase of FM state. The cell parameters are  $a = 14.35$  Å,  $b = 14.46$  Å, i.e., same in  $a$  direction while about 1% stretched in  $b$  directions compared with the  $P\bar{3}m1$  phase ( $a = b = 14.35$  Å). No significant deviation from  $120^\circ$  is found for the  $\gamma$  ( $= 120.25$ ) angle. The calculated bond length of V-V and V-Te is 3.59 Å and 2.71 Å on average. We find the shortest V-V distance of 3.25 Å between the same spins, and the longest distance of 3.98 Å between opposite spins. Such different bond lengths in-

dicates that all the magnetic vanadium atoms are in an irregular octahedron.

For the case of FerriM state with space group  $P3m1$  (156), the formation enthalpy is 9 meV/f.u. lower than  $P\bar{3}m1$  phase. The optimized structural parameters of  $P3m1$  (4 f.u./cell) structure are  $a = b = 7.20$  Å. It has two non-equivalent V atoms (labeled V1 and V2), locating at (0.000 0.000 0.500) and (0.963 0.482 0.500), respectively (as shown in Fig. 2f). The distance between V1 and V2 is 3.61 Å, whereas the bond lengths of V2-V2 have two values (3.21 Å and 4.00 Å). The  $P3m1$  phase can be obtained when the three V atoms of undistorted ( $2 \times 2$ )  $1T-VTe_2$  gathered toward their center. This phenomenon can be explained by charge density wave (CDW) behaviors. Looking at the band structures of primitive  $1T-VTe_2$  (Fig. 1c), there are the semi-metallic overlap between the valence band top at  $\Gamma$  and the conduction band bottom at M,

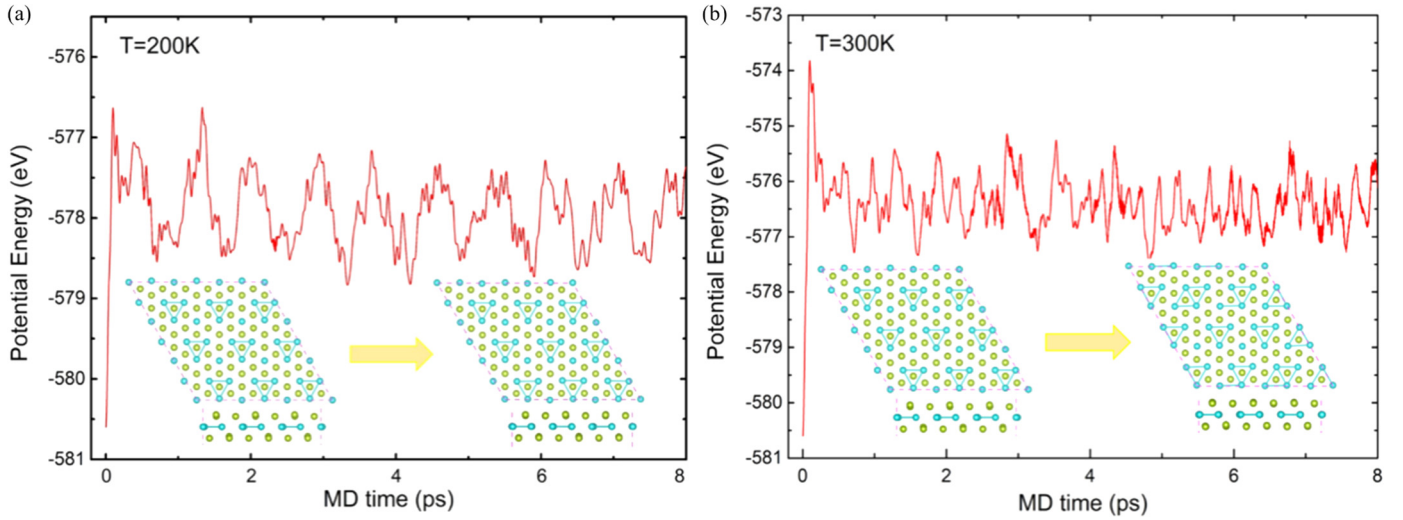


Fig. 3. Evolution of the total energy of  $P3m1$  phase along AIMD simulations with temperature of 200 K (a) and 300 K (b).

which is a critical factor controlling the tendency towards the  $2 \times 2$  distortion [35,36]. Although no phonons with imaginary frequency appear at the M point (see Fig. 1b), an acoustic branch disperses downwards and has the lowest frequency at point M, indicating that the softening of the acoustic branch may cause  $1T-VTe_2$  to become unstable. Therefore, it is likely an unstable phase. In order to determine its kinetic stability, the phonon frequencies of  $P3m1$  structure (Figure S5a) was calculated. No imaginary frequency and no softened phonons was found in the calculated spectra, which demonstrates that  $P3m1$  phase is more stable than  $P\bar{3}m1$  structure.

As for the  $P21/m$  phase with bi-stripe antiferromagnetic state, the formation enthalpy is 9 meV/f.u., lower than the  $F\bar{3}m1$  structure, while it is almost equal to that of  $P3m1$  phase. The optimized lattice constants ( $a = 14.24 \text{ \AA}$ ) for  $P21/m$  phase undergoes about 0.8% contraction, while  $b (= 14.42 \text{ \AA})$  undergoes about 0.5% extension as compared to  $P\bar{3}m1$  phase. The bond length of V-V and V-Te are ranged from 3.36  $\text{\AA}$  to 3.86  $\text{\AA}$  and 2.67  $\text{\AA}$  to 2.77, respectively. Obviously, the distance of V-V between the opposite spins (3.86  $\text{\AA}$ ) is greater than the same spins (demonstrated in Fig. 2d).

Figure S5 displays the calculated phonon spectra of the  $P3m1$ ,  $P21/m$ ,  $C2/m$  phases. No imaginary phonon frequencies in the entire Brillouin zone are found, indicating that they are kinetically stable. To determine the thermal stability, we have carried out *ab initio* molecular dynamics AIMD simulations within the canonical ensemble (NVT) at temperatures of 200 K and 300 K for  $P3m1$  phase, with a supercell containing 108 atoms. At 200 K, almost no distortion is observed after 8 ps (as displayed in Fig. 3a) and the total energy fluctuation no more than 15 meV/atom, confirming its thermal stability. The structure distorts significantly at temperature of 300 K (as shown in Fig. 3b), indicating its instability at room temperature. The result is consistent with its Curie temperature ( $T_c \approx 200 \text{ K}$ ) (as shown in Figure S7).

### 3.3. Electronic and magnetic properties

Magnetic studies show that  $P3m1$  phase prefers FerriM coupling, which is more stable than FM state by an energy difference of 15.7 meV/f.u. The total moment of the  $P3m1$  phase is  $4 \mu_B/\text{f.u.}$ , where V1 and V2 atoms contribute by  $-0.57 \mu_B$  and  $1.53 \mu_B$ , respectively. For the  $C2/m$ ,  $P21/m$  phases, the lattice symmetry is only compatible with the AFM spin ordering. The local magnetic moment of V atom is about  $1.20 \mu_B$  in absolute value for  $C2/m$  and  $1.29 \mu_B$ ,  $1.46 \mu_B$  in absolute value for  $P21/m$ . The spin arrangements on V sites are illustrated in spin charge den-

sity diagram in Fig. 2. Non-magnetic calculations were also performed on the three structures, which were found to relax to the  $P\bar{3}m1$  phase and it is energetically unfavored. Particularly, the lattice symmetry of the three phases is only compatible with their corresponding spin ordering. That is, the lattice as well as the electronic properties will significantly change when the spin ordering changes. These peculiar phenomena provide strong evidence for spin-charge-lattice coupling in  $VTe_2$ .

Magnetic anisotropy energy (MAE) is a crucial property for two-dimensional magnetic materials, maintaining its long range magnetic ordering against thermal fluctuations. Also a large MAE would increase the density of magnetic data storage and provide an opportunity of magnetoelectronic application. To obtain the MAE, noncollinear magnetic calculations were performed for magnetization along three directions, i.e., X[100], Y[010], Z[001], where Z is normal to the surface. We define  $E_{XZ}$  ( $E_{YZ}$ ) as the energy difference between X(Y) and Z directions. All the structures have easy magnetization direction lying in the plane and the MAE of  $P21/m$  phase reaches the maximum value of 1.26 meV/f.u. compared to the other phases:  $P3m1$  ( $\sim 0.31 \text{ meV/f.u.}$ ),  $C2/m$  ( $\sim 0.59 \text{ meV/f.u.}$ ) and  $F\bar{3}m1$  ( $\sim 0.73 \text{ meV/f.u.}$ ).

Structural changes are often accompanied by changes in electronic structure and magnetic properties. It reveals that four phases ( $P\bar{3}m1$ ,  $C2/m$ ,  $P21/m$ ,  $P3m1$ ) of  $VTe_2$  present various magnetic properties and rich electronic natures (Fig. 4 and Fig. 5). For the sAFM  $P\bar{3}m1$  phase, the band dispersion for spin-up and spin-down bands crosses the Fermi Level, indicating that  $P\bar{3}m1$  is an AFM metal (Fig. 3a). Near the Fermi energy, the electronic DOS is dominated by V 3d states, with a little contribution of Te 5p, indicating that there is a slight hybridization between V 3d and Te 5p orbitals. For the  $P21/m$  and  $C2/m$  structures, the band structures (Fig. 4b and Fig. 4c) exhibit semiconducting behavior with indirect bandgaps of 0.11 and 0.07 eV, respectively. For the  $P3m1$  phase, the spin and orbital projected band structures (Fig. 5) obviously demonstrated that the spin-up and spin-down channels are non-degenerate, in which the majority channel exhibits semiconducting natures while the other channel behaves metallic properties. Such particular band structures manifest that it is an intrinsic half-metallic phase that can provide 100% spin-polarization of electrons near the  $E_F$ , ideally for spin injection. The majority spin channel has the band gap as large as 0.37 eV, enough to prevent flips from electrons of minority spin channel. Around the  $E_F$ , the majority electronic states are mainly contributed by V2-3d orbitals, while the minority bands are mainly contributed by V1-d states, both of them have a minor hybridization with Te-5p states. These phe-

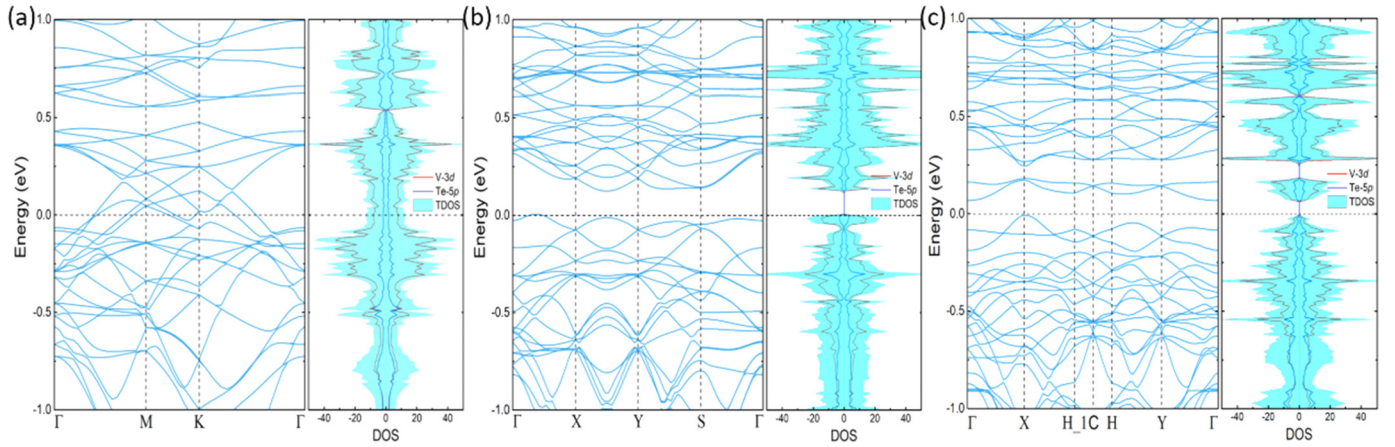


**Fig. 4.** The electronic structures of  $VTe_2$ . (a)  $P\bar{3}m1$  phase (b)  $P21/m$  phase (c)  $C2/m$  phase. The Fermi level or VBM is set to zero, and the unit of electronic density of states is states/eV.

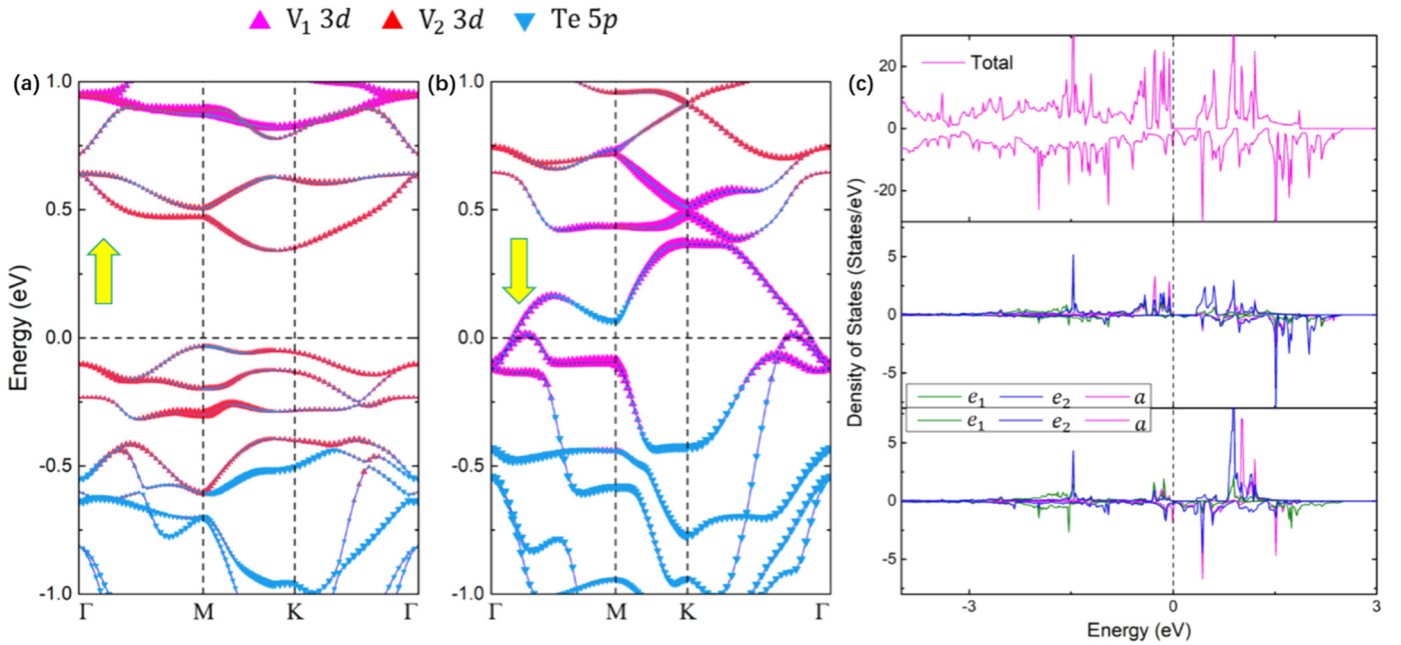


**Fig. 5.** Orbital projected band structures of  $P3m1$  phase with spin-up (a) and spin-down (b) channels. (c) Projected density of  $P3m1$  phase. The Fermi level is set to zero.

nomena will be clearer from a combination with TDOS and PDOS. Under the  $C_{3V}$  symmetry, the 3d orbitals of V atoms split into a non-degenerate ( $dz^2$ ) level and two 2-fold degenerate  $e_1$  ( $dxz/dyz$ ) and  $e_2$  ( $dxy/dx^2 - y^2$ ) levels. At  $E_F$ , no electronic state distribution can be observed in the majority channel, while in the minority channel, only  $V1 e_1$  and  $e_2$  orbitals are fractionally occupied, and the occupation of  $V2-d$  orbitals are negligible.

### 3.4. Magnetic and structure phase transition of monolayer $VTe_2$

Strain is a common means that exists or is easily applied in two-dimensional materials as a control tool to alter the electronic and magnetic properties of the material. Here, we apply strains in different directions to  $P\bar{3}m1$ ,  $C2/m$ ,  $P21/m$ ,  $P3m1$  phases to observe how their structural, magnetic and electronic properties evolve. The biaxial strain defined as  $\varepsilon = (a - a_0)/a_0 \times 100\%$ , where  $a_0$  and  $a$  are the lattice constant of the unstrained and strained monolayer. The uniaxial strain (along  $a$ -axis direction) is that fixing lattice  $a$  at a length of  $(1 + \varepsilon)a_0$  and allowing lattice  $b$  to relax. The energy evolution of the four phases in terms of strain are shown in Figure S6. We can clearly observe that the  $C2/m$  phase is always

energetically favored under uniaxial or biaxial strains of  $-2\%$  to  $2\%$ , suggesting that  $C2/m$  structure and the associated magnetic order remain robust against external strain. For  $P3m1$  FerriM half-metal phase, we also investigate the evolution of the nearest neighbor magnetic exchange parameter  $J$  and magnetic anisotropy energy under biaxial strain. As exhibited in Fig. 6,  $J$  and MAE is sensitive to strain. As the increase of tensile strain, the MAE increases to  $0.56$  meV/V at  $4\%$ , twice than that of without strain ( $0.31$  meV), further confirming the strong interactions between spin and lattice. The first-order spin-lattice coupling strength  $\frac{\partial J_{\mu_1\mu_2}}{\partial \varepsilon_i}$  (where  $J$  is the magnetic exchange parameter between  $\mu_1$  and  $\mu_2$ ,  $\varepsilon_i$  is the strain) is about  $1.25$  meV/% under compress strain, greater than  $CrI_3$  (about  $0.89$  meV/%) [37]. This also provides an evidence of strong spin-lattice coupling effect in  $VTe_2$ . The  $J$  value decreases and then increases under tensile strains, likely being attributed to the competition between superexchange interaction and direct interaction. It strongly depends on the change of angle  $V2-Te-V2$  with the increasing strain.

Carrier doping is another convenient and efficient approach to tune the electronic and magnetic properties of 2D films. Previous work had shown that the magnetization easy axis can be tuned

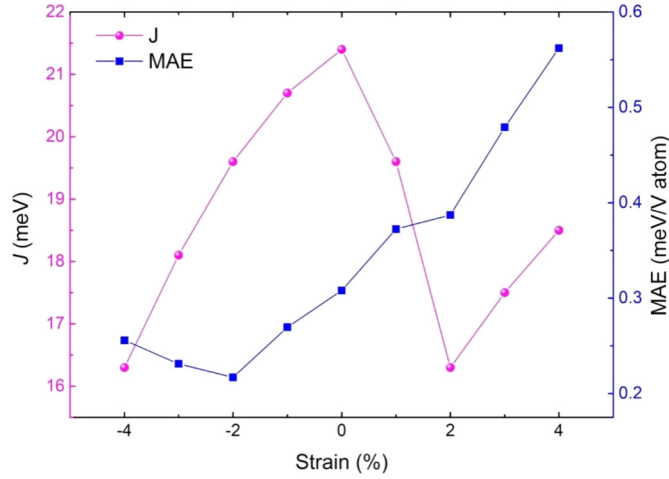


**Fig. 6.** Dependence of the nearest-neighbor exchange parameter  $J$  on the biaxial strain (pink line) for the FerriM half-metal phase. The evolution of corresponding MAE under biaxial strain is depicted in the blue line.

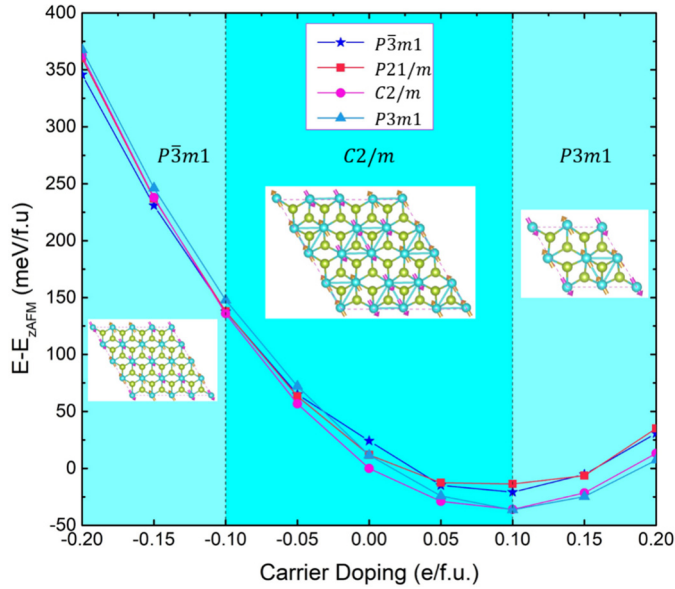


**Fig. 7.** The relative energy changes as a function of carrier concentration with different phases corresponding to different magnetic states. The  $E_{ZAFM}$  is the energy of zAFM  $C2/m$  phase without doping. The positive and negative values are for electron and hole doping, respectively.

from out-of-plane to in-plane by electrostatic doping [38,39]. Additionally, the magnetic transition can be induced by carrier-doping. [40] Fig. 7 displays the relative energy changes as a function of carrier concentration with different phases corresponding to different magnetic states. With the electron doping concentration increases, the energy differences between the zAFM phase of  $C2/m$  and FerriM phase of  $P3m1$  decrease. When the electronic doping is 0.1 e/f.u. ( $\sim 7.7 \times 10^{13} \text{ cm}^{-2}$ ), the FerriM phase of  $P3m1$  is more energy preferable. However, when the hole doping reaches to 0.1 hole/f.u., zAFM  $C2/m$  phase transforms to sAFM  $P\bar{3}m1$  phase. In a pristine  $C2/m$  phase, the Fermi level relative to the vacuum level is calculated to be  $-4.793 \text{ eV}$ , which is higher than the pristine  $P3m1$  ( $-4.896 \text{ eV}$ ). Also, the Fermi level of  $C2/m$  is in the energy gap while the Fermi level of  $P3m1$  is in the valence band. Thus, when electrons are introduced, the energy of  $C2/m$  will decrease less than  $P3m1$ . With the number of electrons increases, the  $P3m1$  will become more energy preferable than  $C2/m$ . Similarly, the valence band of  $C2/m$  is below the Fermi level ( $-4.793 \text{ eV}$ ),  $P\bar{3}m1$

is a metal with Fermi level of  $-4.770 \text{ eV}$ , so more energy is required to introduce holes in  $C2/m$ , which causes  $C2/m$  to become more unstable than  $P\bar{3}m1$  when the concentration of hole doping increases. Experimentally, it is feasible to achieve a carrier concentration reaching  $10^{13} \sim 10^{14} \text{ cm}^{-2}$  in 2D systems [41]. Also, we hypothesize that  $P3m1$  phase with FerriM half-metal properties can be prepared by electron doping by selecting suitable substrates [42]. Hence, electron doping can introduce transitions of structural phase and magnetic state in  $VTe_2$ , leading to a broad application prospect in spintronic devices.

Considering the electron correlation effect in  $VTe_2$  monolayer, we have employed GGA+U method to calculate the evolution of the four phases, with different  $U_{\text{eff}}(U-J)$  from Reference [43]. For convenience,  $U_{\text{eff}}$  is simplified as  $U$  below. The energy difference  $\Delta E = E - E_{\text{min}}$  as a function of  $U$  is depicted in Figure S8. Here,  $E$ ,  $E_{\text{min}}$  are the total energy of different phases with a specific  $U$  and the minimum energy among these phases, respectively. Correspondingly, the structural and magnetic parameters as well as band gap of the four phases under different  $U$  are listed in Table S2, where  $U = 4.3 \text{ eV}$  is evaluated from four phases using first-principles calculations within the linear response approach (Figure S9) [44]. It is obvious that the ground state changes dramatically with the adopted  $U$  value. Meanwhile, the energy difference between each phase is not significant when  $U$  is less than 2.5, while the energy difference increases remarkably when  $U$  is greater than 2.5. In addition, the band gap and lattice constants of each phase change dramatically with the  $U$  value. As there are no enough experimental observation to confirm the various ground states and band gap change, it is hard to determine which value of  $U$  is reasonable. Nevertheless, the results from different  $U$  value also demonstrate the structural, electronic and magnetic diversity of the monolayer  $VTe_2$ . Additionally, GGA is also adopted in earlier studies of  $VSe_2$ , a similar system to  $VTe_2$ , with reasonable results comparing to the experimental observation. [45–47] Therefore, our main results are still based on the GGA results.

#### 4. Conclusion

In summary, we have systematically studied the crystal structures, phonon spectrum, electronic and magnetic properties of 1T- $VTe_2$ . We have demonstrated theoretically that no-distorted 1T- $VTe_2$  exhibits antiferromagnetic metal properties after considering various configurations. Peculiarly, three stable  $VTe_2$  phases,  $P3m1$ ,  $P21/m$ , and  $C2/m$ , are predicted with diverse electronic structures and magnetic properties.  $P21/m$  and  $C2/m$  are AFM semiconductors with indirect gap of 0.11 eV and 0.07 eV, respectively, while  $P3m1$  is a FerriM half-metal with spin up band gap of 0.37 eV. Furthermore,  $VTe_2$  can be transformed from  $C2/m$  AFM semiconductor to  $P3m1$  FerriM metal by electron doping, while hole doping can induce a transition from  $C2/m$  AFM semiconductor to  $P\bar{3}m1$  AFM metal. The various and interesting electronic and magnetic properties of  $VTe_2$  are likely due to the strong coupling of charge, lattice, and spin degrees of freedom in  $VTe_2$ . The diverse electronic and magnetic properties of  $VTe_2$  will provide a good platform for researchers to understand the interactions between spin, charge and lattice.

#### CRedit authorship contribution statement

**Bi-Dan Guo:** Writing – original draft, Visualization, Validation, Methodology, Investigation, Formal analysis, Data curation, Conceptualization. **Ji-Hai Liao:** Conceptualization. **Wen-Qiang Xie:** Visualization. **Yin-Hui Peng:** Visualization. **Yu-Jun Zhao:** Writing – review & editing, Supervision, Software, Resources, Project administration.

## Declaration of competing interest

The authors declare that they have no known competing financial interests or personal relationships that could have appeared to influence the work reported in this paper.

## Acknowledgements

This work is financially supported by National Natural Science Foundation of China (NSFC) (Grant No. 12074126), the Foundation for Innovative Research Groups of NSFC (Grant No. 51621001), the Fundamental Research Funds for the Central Universities (Grant No. 2020ZYGXZR076), Guangdong Basic and Applied Basic Research Foundation (No. 2021A1515010349).

## Appendix A. Supplementary material

Supplementary material related to this article can be found online at <https://doi.org/10.1016/j.physleta.2022.128260>.

## References

- [1] C. Gong, X. Zhang, *Science* 363 (2019), 2019, eaav4450.
- [2] B. Huang, G. Clark, E. Navarro-Moratalla, D.R. Klein, R. Cheng, K.L. Seyler, D. Zhong, E. Schmidgall, M.A. McGuire, D.H. Cobden, W. Yao, D. Xiao, P. Jarillo-Herrero, X.D. Xu, *Nature* 546 (2017) 270.
- [3] S.C. De La Barrera, M.R. Sinko, D.P. Gopalan, N. Sivadas, K.L. Seyler, K. Watanabe, T. Taniguchi, A.W. Tseng, X. Xu, D. Xiao, B.M. Hunt, *Nat. Commun.* 9 (2018) 1427.
- [4] H. Liu, S.X. Huangfu, X. Zhang, H. Lin, A. Schilling, *Phys. Rev. B* 104 (2021) 064511.
- [5] S. Feng, W. Mi, *Appl. Surf. Sci.* 458 (2018) 191.
- [6] C. Wang, Y. An, *Appl. Surf. Sci.* 538 (2021) 148098.
- [7] P.P. Ferreira, A.L.R. Manesco, T.T. Dorini, L.E. Correa, G. Weber, A.J.S. Machado, L.T.F. Eleno, *Phys. Rev. B* 103 (2021) 125134.
- [8] P. Suo, H.Y. Zhang, S.N. Yan, W.J. Zhang, J. Fu, X. Lin, S. Hao, Z.M. Jin, Y.P. Zhang, C. Zhang, F. Miao, S.J. Liang, G.H. Ma, *Phys. Rev. Lett.* 126 (2021) 227402.
- [9] M.Z. Liu, C.W. Wu, Z.Z. Liu, Z.Q. Wang, D.X. Yao, D.Y. Zhong, *Nano Res.* 13 (2020) 1733.
- [10] Y. Wang, J.H. Ren, J.H. Li, Y.J. Wang, H.N. Peng, P. Yu, W.H. Duan, S.Y. Zhou, *Phys. Rev. B* 100 (2019) 241404.
- [11] X.X. Ding, J. Xing, G. Li, L. Balicas, K. Gofryk, H.H. Wen, *Phys. Rev. B* 103 (2021) 125115.
- [12] H.T. Liu, Y.Z. Xue, J.A. Shi, R.A. Guzman, P.P. Zhang, Z. Zhou, Y.G. He, C. Bian, L.M. Wu, R.S. Ma, J.C. Chen, J.H. Yan, H.T. Yang, C.M. Shen, W. Zhou, L.H. Bao, H.J. Gao, *Nano Lett.* 19 (2019) 8572.
- [13] L.V. Begunovich, A.V. Kuklin, M.A. Visotin, A.A. Kuzubov, F.N. Tomilin, A.S. Tarasov, Y.G. Mikhalev, P.V. Avramov, *Appl. Surf. Sci.* 510 (2020) 145315.
- [14] N. Devaraj, N.K. Tarafder, *Phys. Rev. B* 103 (2021) 165407.
- [15] C. Chappert, A. Fert, A.F.N.V. Dau, *Nat. Mater.* 6 (2007) 813.
- [16] L.A. Ponomarenko, F. Schedin, M.I. Katsnelson, R. Yang, E.G. Hill, K.S. Novoselov, A.K. Geim, *Science* 320 (2008) 356.
- [17] R.F. Neumann, M. Engel, M. Steiner, *Nanoscale* 8 (2016) 13652.
- [18] K.F. Mak, K.L. He, J. Shan, T.F. Heinz, *Nat. Nanotechnol.* 7 (2012) 494.
- [19] J.D. Zhou, J.H. Lin, X.W. Huang, Y. Zhou, Y. Chen, J. Xia, H. Wang, Y. Xie, H.M. Yu, J.C. Lei, D. Wu, F.C. Liu, Q.D. Fu, Q.S. Zeng, C.H. Hsu, C. Lyang, L. Lu, T. Yu, Z.X. Shen, H. Lin, B.I. Yakobson, Q. Liu, K. Suenaga, G.T. Liu, Z. Liu, *Nature* 556 (2018) 355.
- [20] C. Ataca, H. Şahin, S. Ciraci, *J. Phys. Chem. A* 116 (2012) 8983.
- [21] W. Chen, J.M. Zhang, Y.Z. Nie, Q.L. Xia, G.H. Guo, *J. Magn. Magn. Mater.* 508 (2020) 166878.
- [22] J. Li, B. Zhao, P. Chen, R.X. Wu, B. Li, Q.L. Xia, G.H. Guo, J. Luo, K.T. Zang, Z.W. Zhang, H.F. Ma, G.Z. Sun, X.D. Duan, X.F. Duan, *Adv. Mater.* 30 (2018) 1801043.
- [23] K. Sugawara, Y. Nakata, K. Fujii, K. Nakayama, S. Souma, T. Takahashi, T. Sato, *Phys. Rev. B* 99 (2019) 241404.
- [24] T. Dai, S.D. Kang, X.Y. Ma, S. Dang, H.W. Li, Z.L. Ruan, W.Q. Zhou, P. Hu, S.W. Li, S.X. Wu, *J. Phys. Chem. C* 123 (2019) 18711.
- [25] D. Won, D.H. Kiem, H. Cho, D. Kim, Y. Kim, M.Y. Jeong, C. Seo, J. Kim, J.G. Park, M.J. Han, H. Yang, S. Cho, *Adv. Mater.* 32 (2020) 1906578.
- [26] J. Furthmüller, G. Kresse, *Phys. Rev. B* 54 (1996) 11169.
- [27] G. Kresse, J. Furthmüller, *Comput. Mater. Sci.* 6 (1996) 15.
- [28] P.E. Blochl, *Phys. Rev. B* 50 (1994) 17953.
- [29] D. Joubert, G. Kresse, *Phys. Rev. B* 59 (1999) 1758.
- [30] J.P. Perdew, K. Burke, M. Ernzerhof, *Phys. Rev. Lett.* 77 (1996) 3865.
- [31] S. Baroni, S.D. Gironcoli, A.D. Corso, *Rev. Mod. Phys.* 73 (2001) 515.
- [32] A. Togo, I. Tanaka, *Scr. Mater.* 108 (2015) 1.
- [33] V. Wang, N. Xu, J.C. Liu, G. Tang, W.T. Geng, *Comput. Phys. Commun.* 267 (2021) 108033.
- [34] C.C. He, J.H. Liao, S.B. Qiu, Y.J. Zhao, X.B. Yang, *Comput. Mater. Sci.* 193 (2021) 110386.
- [35] B. Guster, R. Robles, M. Pruneda, E. Canadell, P. Ordejón, *2D Mater.* 6 (2018) 015027.
- [36] T.M. Rice, G.K. Scott, *Phys. Rev. Lett.* 35 (1975) 120.
- [37] J. Li, S. Feng, P.S. Wang, E.J. Kan, H.J. Xiang, *Sci. China, Phys. Mech. Astron.* 64 (2021) 286811.
- [38] A.N. Ma, P.J. Wang, C.W. Zhang, *Nanoscale* 12 (2020) 5464.
- [39] X.Z. Li, S.L. Ji, S.S. Li, P. Liu, H. Wu, W. Niu, H.Y. Wang, F. Li, *Phys. Lett. A* 433 (2022) 128000.
- [40] J. Zhou, Q. Sun, *Nanoscale* 6 (2014) 328.
- [41] A.S. Dhoot, C. Israel, X. Moya, N.D. Mathur, R.H. Friend, *Phys. Rev. Lett.* 102 (2009) 136402.
- [42] J.Q. Dai, J. Yuan, C. Ke, Z.C. Wei, *Appl. Surf. Sci.* 547 (2021) 149206.
- [43] S.L. Dudarev, G.A. Botton, S.Y. Savrasov, C.J. Humphreys, A.P. Sutton, *Phys. Rev. B* 57 (1998) 1505.
- [44] M. Cococcioni, S. de Gironcoli, *Phys. Rev. B* 71 (2005) 035105.
- [45] P.K.J. Wong, W. Zhang, F. Bussolotti, X.M. Yin, et al., *Adv. Mater.* (2019) 1901185.
- [46] J. Feng, D. Biswas, A. Rajan, M.D. Watson, F. Mazzola, et al., *Nano Lett.* 18 (2018) 4493–4499.
- [47] G. Duvjir, B.K. Choi, I. Jang, S. Ulstrup, S. Kang, T. Thi Ly, et al., *Nano Lett.* 18 (2018) 5432–5438.